ELSEVIER

Contents lists available at ScienceDirect

# Journal of Power Sources

journal homepage: www.elsevier.com/locate/jpowsour





# Advanced manufacturing of thin-film lithium metal anode by pulsed-laser deposition for next-generation solid-state batteries

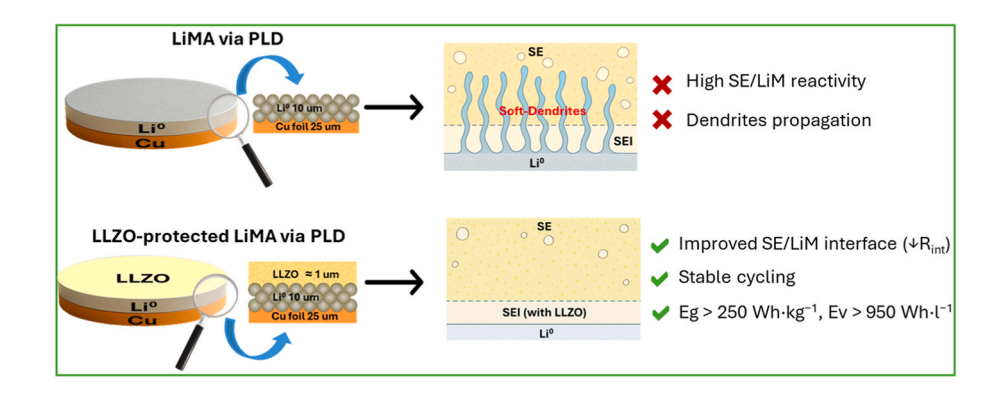
Nico Zamperlin <sup>a</sup>, Rosalía Cid <sup>a</sup>, Ville Kekkonen <sup>b</sup>, Arianna Pesce <sup>a</sup>, Manar Cheddadi <sup>a</sup>, Beatriz M. Gomes <sup>c,d</sup>, Manuela C. Baptista <sup>c,d</sup>, M. Helena Braga <sup>c,d</sup>, Ander Orue <sup>a,\*</sup>, Pedro López-Aranguren <sup>a</sup>

- <sup>a</sup> Center for Cooperative Research on Alternative Energies (CIC EnergiGUNE), Basque Research and Technology Alliance (BRTA), Alava Technology Park, Albert Einstein, 48, 01510, Vitoria-Gasteiz, Spain
- <sup>b</sup> PULSEDEON Oy, Technology Center, Piisilta 1, Ii, Finland
- <sup>c</sup> Engineering Faculty, University of Porto, R. Dr. Roberto Frias s/n, 4200-465, Porto, Portugal
- d LAETA, Institute of Science and Innovation in Mechanical and Industrial Engineering, R. Dr. Roberto Frias 400, 4200-465, Porto, Portugal

#### HIGHLIGHTS

- PLD enables precise lithium metal anode fabrication for solid-state batteries.
- Sequential deposition of lithium metal and LLZO layers achieved via PLD.
- LLZO coating enhances interfacial stability and extends cycling life.
- PLD-Li anode integrated with NMC cathode shows promising cycling performance.

#### GRAPHICAL ABSTRACT



# ARTICLE INFO

Keywords:
All-solid-state batteries
Pulsed-laser deposition
Lithium metal anode
Sulfide solid electrolyte
Interfacial stability
Lithium lanthanum zirconium oxide

# ABSTRACT

All-solid-state batteries (ASSBs) offer improved safety, energy density, and cycling stability compared to conventional lithium-ion batteries. Sulfide-based electrolytes stand out for their high ionic conductivity and ease of processing, though interfacial instability and lithium dendrite formation remain major challenges. This study explores Pulsed-Laser Deposition (PLD) as a precise and versatile technique to fabricate thin lithium metal anodes and conformal protective coatings. A 10 µm lithium layer and a 1 µm lithium lanthanum zirconium oxide (LLZO) layer are sequentially deposited on copper foil using PLD. The LLZO coating enhances interfacial stability with sulfide electrolytes, improving cycling performance. Unlike conventional fabrication methods, PLD enables controlled deposition of thin lithium metal anodes, contributing to higher energy density in ASSBs. Structural, microstructural and electrochemical characterizations confirm the high quality of both layers. Symmetric cell testing reveals that lithium anodes, both bare and LLZO-coated, cycle stably with low polarization. The LLZO interlayer reduces interfacial resistance and mitigates lithium dendrite growth, extending the cycle life. These

E-mail address: aorue@cicenergigune.com (A. Orue).

<sup>\*</sup> Corresponding author.

results highlight PLD as a scalable and effective approach for engineering lithium metal anodes with tailored protective coatings, improving interfacial compatibility with sulfide-bases solid electrolytes and advancing the development of next-generation ASSBs.

#### 1. Introduction

All-solid-state batteries (ASSBs) have emerged as a transformative technology in the field of energy storage, offering significant advantages over conventional lithium-ion batteries. By replacing the flammable liquid electrolyte with a solid electrolyte (SE), ASSBs promise improved safety, increased energy density, and faster charging capabilities [1]. Among the various SE candidates, garnets [2], halides [3,4] and sulfides [5] have garnered considerable attention. The latter ones are a promising class of materials for next-generation batteries due to their outstanding ionic conductivity — often exceeding 10<sup>-3</sup> S·cm<sup>-1</sup> — and their favorable mechanical softness, which enhance interfacial contact with electrode materials [6]. To obtain ASSBs with high energy densities, recently research has focused on integrating sulfides SEs with thin lithium metal anode (LiMA), or even anode-free configuration [7,8]. Thanks to their exceptionally high theoretical specific capacity of 3860 mAh·g<sup>-1</sup> and 2050 mAh·l<sup>-1</sup>, LiMA is considered one of the most promising anodes for next-generation ASSBs [7,9,10]. Moreover, avoiding excess lithium as used in conventional designs can significantly enhance the overall energy density of the resulting cells [11,12]. Nonetheless, safety limitations continue to be a major obstacle to the large-scale adoption of LiMA in ASSBs technology. The primary limitation arises from their high reactivity and tendency to form lithium dendrites, which can lead to internal short circuit and premature battery failure [13–15]. Additionally, the interfacial stability between lithium and sulfide SEs remains a critical challenge, as chemical decomposition at the interface can produce byproducts such as Li<sub>2</sub>S, Li<sub>3</sub>P, LiCl, and polysulfides [16]. This instability is influenced by multiple factors including the specific composition of the sulfide electrolyte, the surface condition of the lithium metal (LiM), and operating conditions, though the main contribution is related to LiMA|SE interface itself [16,17]. To address this challenge, strong efforts have been directed towards stabilizing the LiM|SE interface. The strategies, include compositional tuning of the sulfide electrolytes [18], engineering the interface microstructure [19], applying interlayers or protective coatings [20,21], and modifying the LiM surface [19].

State-of-the-art fabrication of LiM foils typically relies on extrusion followed by mechanical rolling to produce freestanding, self-supporting lithium films [22,23]. While lamination of LiM onto copper (Cu) substrates has been explored, conventional processing techniques still face substantial limitations in handling lithium foils thinner than 50  $\mu$ m [8]. In contrast to these top-down approaches, emerging bottom-up approaches such as those based on physical vapor deposition techniques offer a promising alternative, enabling the deposition of high-purity lithium layers with excellent thickness uniformity [8,24,25]. Pulsed-Laser Deposition (PLD) offers several distinct advantages for the synthesis and controlled deposition of thin films [26], making it an interesting method for fabricating thin lithium-based anodes for ASSBs. PLD gives precise control over the composition and stoichiometry, even for complex multicomponent systems [26], while maintaining high deposition rates, making it suitable for scalable manufacturing [27]. Its versatility allows for the deposition of a wide range of materials, including metals, oxides, semiconductors, and organic compounds [28–30], and it is capable of producing films with excellent crystallinity and microstructure quality [26,31,32]. Furthermore, PLD supports the manufacturing of epitaxial films, where the deposited material maintains the same crystal structure and orientation as the underlying substrate. Although several anode materials such as SnO2 and TiO2 layers [33], NiO [34] or even LiM itself [35], have been deposited using PLD, the simultaneous deposition of LiM and a protective coating in a

single-step process remains unexplored. Such an approach would simplify processing, reduce interface defects, and enhance scalability. Among various protective materials, lithium lanthanum zirconium oxide (LLZO) has demonstrated enhanced cyclability when used as an additive in polymer-based electrolytes cells [36], and more recently, in ceramic-based ASSBs, where the oxide/argyrodite combination has shown to be beneficial for interface impedance and electrochemical performance [37,38]. Although LLZO has already been successfully deposited using PLD [28], applying it as a protective layer directly onto LiM and achieving the pure, highly-conductive cubic phase without post-annealing remains a notable challenge. In fact, even if PLD provides precise control over film deposition, the complex phase formation and crystallization processes of LLZO require careful optimization of deposition parameters or the application of post-deposition thermal treatments.

In this work, we present a novel one-step PLD approach for producing on thin and homogeneous LiMA directly onto 25 µm thick Cu substrate for use in ASSBs. This bottom-up method enables higher energy densities compared to conventional LiM processing techniques. By utilizing a multi-target PLD system, both a LiM layer (10  $\mu$ m) and a LLZO protective coating (1 µm) were successfully deposited in a single processing step, fastening fabrication and enhancing process scalability. Two types of Li-on-Cu films were fabricated and compared: bare lithium films and LLZO-protected lithium films. Electrochemical testing in symmetric cell configuration using a sulfide SE demonstrated a contained impedance evolution over time for both anode types and longerterm cycling stability for the LLZO-protected LiMA with no significant potential increase over time. As proof of concept, the PLD-manufactured anodes were integrated into full cells with lithium nickel manganese cobalt oxide (NMC) cathodes, to validate their viability for practical applications. These results highlight the effectiveness and versatility of PLD in producing high-quality, ultrathin LiMA with engineered interfaces. The demonstrated one-step deposition strategy provides a promising pathway for scalable manufacturing of protected lithium anodes, accelerating the development of next-generation ASSBs.

# 2. Experimental

# 2.1. Materials

Li metal anodes were fabricated via PLD at Pulsedeon Oy. The Li targets for the PLD process were prepared from high-purity Li metal rods (99.9 %, Merck). Without breaking the vacuum, a protective LLZO coating was sequentially deposited onto the Li-metal layer within the same PLD process. The LLZO was synthesized from Li<sub>2</sub>CO<sub>3</sub>, La<sub>2</sub>O<sub>3</sub> and ZrO<sub>2</sub> precursors via solid-state reaction method and sintered into pellets which were further processed into PLD targets. A 25 µm-thick Cu foil was used as substrate material for the bilayer deposition. Prior to the process, the Cu sheets were cleaned using acid and solvent baths to remove any surface contaminants and laser-cut with the desired final size and shape. The cleaned substrates were held on a deposition mask and dried under vacuum. Coin-cell electrode samples with Li-layers in thickness of  ${\approx}10~\mu m$  and  ${\approx}1~\mu m$  of LLZO were produced in vacuum conditions (p  $< 5.10^{-6}$  mbar) using picosecond-pulsed laser at wavelength of 532 nm. The PLD deposition setup consisted of a laser source, laser optics and a vacuum chamber equipped with instrumentation for target and substrate manipulations. During deposition, the substrate is moved in the horizontal plane under the material plume ejected from the target, ensuring the formation of a uniform coating layer. A schematic representation of the PLD process is represented in Fig. 1. An example of the fabricated PLD-Li-on-Cu bilayer samples is provided in Fig. S1, illustrating the  $\approx\!10$  µm Li layer on Cu foil using the described PLD approach. Li<sub>6</sub>PS<sub>5</sub>Cl (LPSC) solid electrolyte (LPSCl fine, NEI Corp.,  $\approx\!1$  µm particle size) was employed as the separator for the fabrication of both symmetric and full solid-state cells. The composite cathode was prepared by homogenizing LPSC with LiNi<sub>0.9</sub>Mn<sub>0.05</sub>Co<sub>0.05</sub>O<sub>2</sub> (NMC90505; Huayou New Energy Technology) as the active material, and Super C65 conductive carbon black (Imerys Graphite & Carbon) as the conductive agent.

#### 2.2. Material characterization of Li-on-Cu anodes produced by PLD

## 2.2.1. Scanning electron microscopy (SEM)

Microstructural characterization was carried out using a Hitachi Model S-4800 Field Emission Scanning Electron Microscope to confirm the thickness and surface quality of the Li and LLZO-coated Li samples on steel substrates. The analysis was conducted with an accelerating voltage of 3 kV. The parameters applied were 3 kV acceleration voltage and mixed signal from upper and lower detectors for secondary electrons. Cross sections of the samples were obtained by bending the steel sample until it fractured. This method elongates the lithium layer and forms a wedge shape perpendicular to the cross-section surface, which must be considered during the image analysis. FEI Quanta FEG-200 scanning electron microscope was used for energy-dispersive X-rays spectroscopy (EDX) to qualitatively confirm the presence of LLZO on sample surface. The analysis was performed under an acceleration voltage of 20-30 keV, utilizing secondary electrons and/or backscattered electrons as the primary signals for microscopic images. Magnifications ranging from 1000x to 5000x were employed to examine the surface morphology.

# 2.2.2. Raman spectroscopy

Raman spectra were acquired in the range 100–2000 cm<sup>-1</sup> at room temperature using a Renishaw InVia confocal Raman microscope. A 532 nm wavelength laser was employed as excitation source, with the beam focused through an inverted Leica microscope using 50x objective lens.

# 2.2.3. X-ray diffraction (XRD)

XRD measurements were conducted using a PANalytical Empyrean Series 2 diffractometer equipped with Cu K $\alpha$  radiation source ( $\lambda=1.54443~\mbox{Å}).$  The data were collected within a  $2\theta$  range of  $10^{\circ}-100^{\circ}$ , with a step size of  $0.02^{\circ}$  and scan step time 67 s. The interpolated step size was determined to be 0.026. Data analysis was performed using High-Score Plus software, with reference patterns sourced from the International Centre for Diffraction Data (ICDD) database. The peak analysis yielded a maximum peak significance of 2.2, with peak widths ranging from 0.1 to 0.97.

#### 2.2.4. X-ray photoelectron spectroscopy (XPS)

The surface composition of Li coated Cu foils was analyzed using Xray photoelectron spectroscopy (XPS). To preserve the sample integrity, the samples were transferred from the glove box to the XPS chamber using an Ar-filled airtight transfer tool. The measurements were conducted with a Phoibos 150 XPS spectrometer (SPECS GmbH) installed in an ultra-high-vacuum (UHV) chamber with a base pressure of  $5\cdot10^{-10}$ mbar. A non-monochromatic Mg source ( $h\nu_{K\alpha} = 1253.6$  eV) was employed at low power (100 W). Spectra were acquired in fixed analyzer transmission (FAT) mode with an approximate 2 mm field of view. High resolution spectra were obtained using a pass energy (Epass) of 30 eV and an energy step (E<sub>step</sub>) of 0.1 eV. A Shirley background was subtracted to remove the inelastically scattered photoelectrons signal, and Voigt profiles (70 % Gaussian, 30 % Lorentzian) were used as line shapes. Quantitative analysis was performed by applying tabulated Scofield cross-sections [39], along with correction factors accounting for the energy-dependent analyzer transmission, and variations in effective attenuation length (EAL) of the collected photoelectrons [40].

# 2.3. Preparation of symmetric and full cells

The method used to densify LPSC sulfide electrolyte is described elsewhere [41]. Briefly, 35-40 mg of LPSC powder were weighed and placed into a 6 mm round easy-retrieve pellet die (Across International, W18Cr4V hardened carbon tool steel). A pressure of 360 MPa was then applied for a couple of minutes with manual hydraulic press (Specac, 15 Ton). For the fabrication of symmetric Li-on-Cu cells, a 6 mm diameter Li-on-Cu electrode was positioned on both sides of the solid electrolyte. The entire stack was then transferred back to the pellet die and pressed using a hydraulic press. The same procedure was applied to the Li-on-Cu electrodes protected by a LLZO layer. The resulting symmetric cells were then assembled in a coin cell CR2032 type for electrochemical analysis [41]. The samples were labelled as PLD\_Li\_on\_Cu and PLD\_Li\_on\_-Cu\_LLZO, respectively. For the fabrication of NMC-based full cells, the composite cathode was prepared by mixing LPSC, NMC90505 and Super C65 carbon black in a weight ratio of 40:57:3. The mixture was ground manually in an agate mortar for 15 min to ensure homogeneity. During cell assembly, 30-35 mg of LPSC solid electrolyte powder was first pre-compacted at about 100-150 MPa. Then, ≈5 mg of composite cathode was evenly distributed on the electrolyte surface and co-pressed with the electrolyte under a stepwise pressure sequence of 300–450-600 MPa, maintaining each pressure for 2 min [42]. The cathode areal loading was set at ≈2 mAh·cm<sup>-2</sup>, and PLD\_Li\_on\_Cu\_LLZO electrodes were used as the anode.

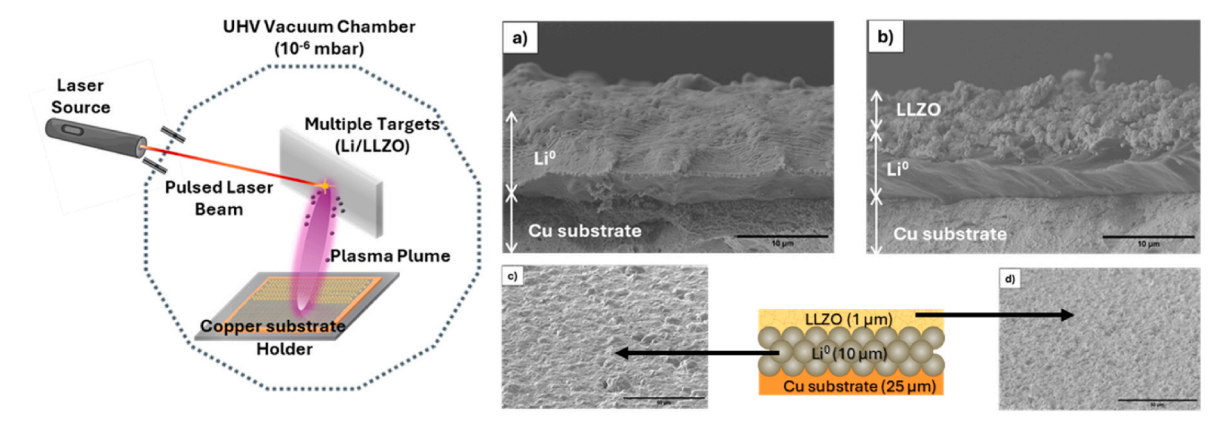


Fig. 1. Left: Scheme of PLD technique to produce LiMA. Right: SEM micrographs of: A) PLD\_Li\_on\_Cu (cross section); B) PLD\_Li\_on\_Cu\_LLZO (cross section); C) PLD\_Li\_on\_Cu (top view); D) PLD\_Li\_on\_Cu\_LLZO (top view). A schematic representation of the multilayer structure is also reported.

#### 2.4. Electrochemical characterization

Electrochemical impedance spectroscopy (EIS) was carried out on symmetric cells incorporating Li-on-Cu electrodes (both bare and LLZOcoated), assembled in a CR2032 coin cell configuration. The measurements, performed at room temperature, utilized Solartron 1260 FRA module, with alternating current (AC) frequencies spanning from 32 MHz to 1 Hz, recording 20 data points per decade, and applying 20 mV excitation amplitude. However, the fitting was done starting from 3 MHz to avoid the inductive contribution of the testing system. Critical current density (CCD) measurements were carried out on symmetric Li-on-Cu LPSC | Li-on-Cu (bare and LLZO-coated) cells from 0.1 to 4 mA·cm<sup>-2</sup> maintaining a fixed capacity of 0.2 mAh·cm<sup>-2</sup>. Stripping-plating (ST-PT) tests were conducted on symmetric Li-on-Cu | LPSC | Li-on-Cu (bare and LLZO-coated) cells, also assembled in CR2032 configuration, as described elsewhere [41]. This analysis provided insights into cell polarization, lithium deposition and dissolutions kinetics, as well as dendritic propagation. These measurements were performed in chronopotentiometry cyclic mode at a constant current density of 0.1 mA·cm<sup>-2</sup>, with a capacity of 0.2 mAh·cm<sup>-2</sup>, using a Biologic VMP-3e potentiostat. EIS was acquired every five cycles with AC frequencies ranging from 1 MHz to 100 mHz, applying a 20 mV excitation amplitude. The cycling performance of NMC-based full cells was evaluated on a Neware-CT-4008Tn-5V-20 mA battery tester and/or Biologic VMP-3e potentiostat, at a rate of 0.05C within a voltage window of 2.6 V and 4.3 V (vs Li/Li<sup>+</sup>) at room temperature.

#### 3. Results and discussion

#### 3.1. Scanning electron microscopy

Fig. 1A-D shows both the top-view and the cross-section micrographs of the two types of LiMAs that are the subject of this study together with a schematization of the multilayer structure. The PLD Li on Cu sample (Fig. 1A and C) exhibits a homogeneous surface with low roughness, as indicated by the low contrast of the top-view image (Fig. 1C) and further confirmed by the cross-section view (Fig. 1A). The cross-sectional images of both bare and LLZO-coated LiMAs (Fig. 1A-B) confirm that the Li thickness is  $\approx$  10  $\mu m$  and Li thickness is also demonstrated to be very homogeneous through the sample. Tiny black spots observed Fig. 1C are probably due to dust or dirtiness accumulated during the handling and sample preparation, or to residual moisture leading to the formation of compounds such as LiOH and Li<sub>2</sub>CO<sub>3</sub>, as confirmed by Raman and XPS (see following sections). The LLZO-protected sample shows a markedly different morphology. The top-view and cross-section micrograph of PLD Li on Cu LLZO (Fig. 1B and D) reveals a uniform surface and the roughness seems to be increased if compared to the non-protected sample due to the presence of LLZO. LLZO is homogeneously distributed on all the surface (Fig. 1D); no depletion zones or region with higher LLZO abundancy could be detected by SEM imaging. The LLZO layer is clearly visible in Fig. 1B; its thickness is in the range of  $\approx 1~\mu m$  but it is challenging to correctly evaluate it due to the sample preparation for the cross-sectional imaging (see materials and methods section). However, also in this case, the thickness of the LLZO layer is confirmed to be very homogeneous through the sample. EDX performed on both the surface and crosssection (Fig. S2A and S2B) confirms the presence of characteristic La and Zr signals, verifying the successful deposition of the LLZO garnet layer onto the lithium surface. The consistent elemental composition observed across multiple regions indicated that the LLZO layer was homogenously deposited throughout the entire sample. Additionally, small peak ascribed to Cu is also detected, proving that the protective layer (Li + LLZO) is relatively thin, as confirmed in the cross-section (Fig. 1B). Overall, SEM analysis highlights the effectiveness of PLD technology in fabricating LiMA with precise control over thickness and surface uniformity. The ability of PLD to produce thin lithium layers

with excellent homogeneity, as well as build well-defined multilayer structures demonstrates its potential as an advanced deposition method for next-generation LiMA. The reduced Li thickness, associated with high homogeneity (compared to conventional methods) can be helpful to provide a more stable increase in the specific gravimetric energy density as well.

#### 3.2. Raman spectroscopy

Fig. 2A shows the Raman spectra of the samples in the range 100–2000 cm<sup>-1</sup>. Both spectra exhibit similar peak positions, indicating that the fundamental chemical composition remains largely unchanged between the two samples. However, variations in peaks intensity between the two spectra could be related to some lack of interaction between lithium and the LLZO protective layer, which may influence the formation or stability of certain species. Looking at the spectra of PLD\_Li\_on\_Cu, the first dominant signal appears approximately at 500 cm<sup>-1</sup>, and this is consistent with Raman spectra of standard Li<sub>2</sub>O, a wellknown oxidation product of lithium [43-45]. A small shoulder observed at 636 cm<sup>-1</sup> and a weak signal at 284 cm<sup>-1</sup> are attributed to the presence of LiOH [43–45], suggesting that the sample may have undergone limited exposure to oxygen and moisture, possibly during handling in the glovebox or sample transfer. The formation of LiOH is commonly associated with lithium reacting with residual water in the environment. The next typical signals are located at 850 cm<sup>-1</sup> and 951 cm<sup>-1</sup>, corresponding to Li<sub>2</sub>CO<sub>3</sub> [46] and Li<sub>2</sub>O<sub>2</sub> [47], respectively. Li<sub>2</sub>CO<sub>3</sub> formation is expected since lithium carbonate naturally forms as a passivation layer on lithium surface upon exposure to air and this has been previously reported during the process of lithium oxidation [46]. Likewise, Li<sub>2</sub>O<sub>2</sub> is a known byproduct of lithium oxidation. The intensities of these peaks suggest that both products are the most abundant species on the lithium surface. A weak band at 1300 cm<sup>-1</sup> is likely associated with the deformation of the hydroxyl bond [48], further confirming the presence of LiOH. A slight shoulder is detected around 910 cm<sup>-1</sup> that may be ascribed to oxalates [49], however the spectra region between 1300 and 1650 cm<sup>-1</sup>, where main Raman peaks of oxalates (Li<sub>2</sub>C<sub>2</sub>O<sub>4</sub>) typically appear, does not show significant features [49], indicating that even if present, these species are not dominant. A distinct peak at 1850 cm<sup>-1</sup> assigned to the stretching vibration of  $C \equiv C$  bond of  $\text{Li}_2\text{C}_2$  (lithium carbide), suggests that the lithium carbonate passivation layer initially present on lithium surface may have undergone partial laser-induced decomposition during measurement, transforming into  $Li_2C_2$  and  $O_2^2$ (Li<sub>2</sub>O). Such transformation has been previously reported [46], and may explain the reduced intensities of the bands at 850 cm<sup>-1</sup> and 951 cm<sup>-</sup> in the LLZO-protected Li-on-Cu. The Raman spectrum of PLD\_Li\_on\_-Cu LLZO closely resembles that of the non-protected sample but with generally lower intensity, which may indicate that the LLZO protective layer may partially mitigate the exposure to the air and reduce the extent of passivation layer. Nevertheless, key characteristics of the previously mentioned lithium compounds are still present, but this could be related to the fact that LiOH and Li<sub>2</sub>CO<sub>3</sub> can still form on top of LLZO (in minor amount), while other peaks can be related to Li-M bonds in LLZO. Therefore, it is important to note that the Raman spectra may not accurately reflect the native solid electrolyte interphase (SEI) composition under working cell conditions. Instead, the data are more likely to capture surface species formed during post-fabrication due to residual environmental exposure.

Likewise, Raman spectroscopy is often used also for LLZO phase identification (cubic/tetragonal). Unfortunately, due to the overlapping of most of the bands assigned to lithium it is difficult to use Raman spectroscopy for the phase identification (and quantification) of LLZO. Furthermore, the Raman spectra of cubic-LLZO usually presents broader bands with respect to tetragonal-LLZO making the identification in this case even more challenging. Nonetheless, the peak at approximately 645 cm<sup>-1</sup> observed in the PLD\_Li\_on\_Cu\_LLZO spectrum, corresponds to the stretching vibration of Zr-O bond and evidences the presence of the

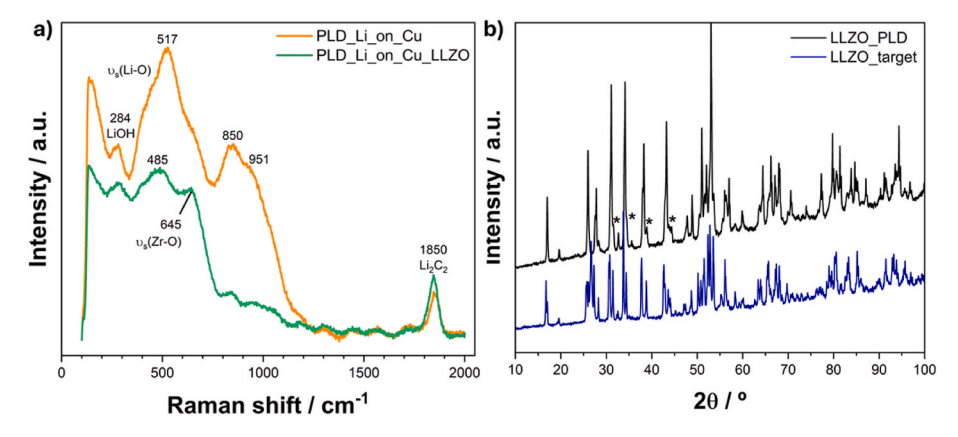


Fig. 2. A): Raman spectrum of PLD\_Li\_on\_Cu and PLD\_Li\_on\_Cu\_LLZO; B) XRD patterns of PLD-deposited LLZO and of the LLZO target.

high-conductive cubic-LLZO phase [50], indicating that at least part of the LLZO remains in its cubic phase.

# 3.3. X-ray diffraction

X-ray diffraction patterns of LLZO deposited by PLD and of the LLZO target used during deposition are shown in Fig. 2B. The slight peak shifting between the two patterns is likely due to the difference in sample forms during XRD analysis: in fact, PLD film material was in flake form and when placed in the XRD holder could not be placed at the same height as standard powder, introducing an apparent 20 shift. Considering this, the pattern of LLZO PLD is consistent with the one of the LLZO target indicating that LLZO is successfully deposited. LLZO can present two main phases, the cubic (ICDD 04-028-4220) and the tetragonal (ICDD 04-029-0339). For battery-like applications the cubic phase is the preferred one since it has higher ionic conductivity [51], however, it has been previously reported being very challenging to obtain a pure cubic LLZO phase through PLD [51] because it requires a very precise control over the deposition parameters such as substrate temperature, oxygen partial pressure and so on. According to the literature, the tetragonal phase is more stable at lower temperature and may form during PLD if the deposition conditions are not perfectly optimized. The diffraction patterns of the cubic and tetragonal phase of LLZO mainly differ in peaks that are singlets for the cubic phase (due to its symmetry) and doublets for the tetragonal one [52]. Accordingly, the pattern of LLZO deposited by PLD is most likely resulting from a mixture of cubic and tetragonal phases since most of the main peaks are neither singlet nor doublets but clearly present shoulders (marked with \* in Fig. 2B). In addition to that, the intense peak at about 28° is probably due to the presence of La<sub>2</sub>Zr<sub>2</sub>O<sub>7</sub> or other similar impurities, common byproducts when depositing LLZO by PLD [53,54]. In any case, XRD results prove the successful deposition of LLZO, which is also partially present in its highly conductive cubic form, supporting the conclusions

from Raman analysis. With an optimization of deposition parameters, it could be possible to further stabilize the cubic phase minimizing at the same time unwanted byproducts such as  $\text{La}_2\text{Zr}_2\text{O}_7$ . These adjustments are currently being the subject of further studies.

#### 3.4. X-ray photoelectron spectroscopy

Fig. 3 shows the XPS analysis of PLD Li on Cu samples, peaks info and relative areas are listed in Table S1 in supporting information. XPS analysis provides complementary insights into the chemical composition of the passivation layer formed on the PLD-deposited lithium and corroborates some of the findings of Raman spectroscopy. The deconvolution of the peaks associated with O 1s, C 1s, and Li 1s reveals that LiOH and Li<sub>2</sub>C<sub>2</sub>O<sub>4</sub> are the main passivation products, suggesting that surface oxidation may follow a slightly different pathway than that observed in Raman analysis. It is worthy to mention that XPS is a very surface sensitive technique, with a probing depth typically below 10 nm, being able to detect only the uppermost layer of the samples, whereas Raman spectroscopy can monitor a significantly higher depth of the material. Accordingly, while Raman spectroscopy detects Li<sub>2</sub>CO<sub>3</sub>, it is not significantly observed in XPS, implying that it could be present in the subsurface but may not dominate the extreme surface layer. Another possible explanation could be related to carbonate formation and further decomposition during Raman analysis due laser heating as reported in literature [46] or due to a comparatively less effective sealing than in XPS, so that we cannot fully exclude the presence of trace O2 or CO2 during measurement. Such residual gases, even at very low concentrations, have been shown in literature to rapidly form Li<sub>2</sub>CO<sub>3</sub> layers on metallic Li surfaces [55]. Furthermore, the detection of a clear LiM peak suggests that the passivation layer is very thin, with a thickness below the typical 10 nm of maximum probing depth in XPS. This implies that the passivation layer does not significantly hinder electron penetration, supporting the hypothesis of a more uniform and controlled oxidation

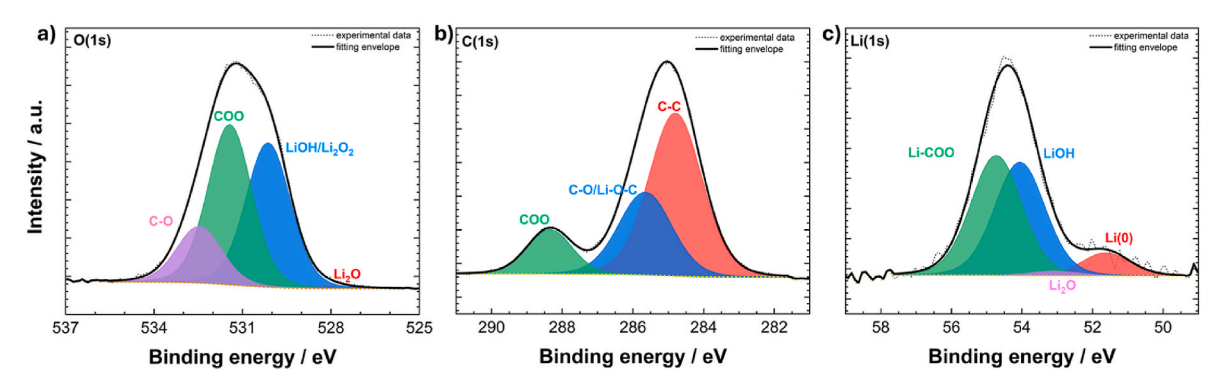


Fig. 3. XPS elemental analysis of PLD Li on Cu sample: A) O(1s), B) C(1s) and C) Li(1s).

process in PLD-derived lithium films. A comparison with commercial lithium foils produced via mechanical method (Fig. S3) reveals notable differences in the passivation chemistry. The passivation layer formed on lithium deposited by PLD is thinner and exhibits a different composition, being richer in LiOH while lacking Li<sub>2</sub>CO<sub>3</sub>, which is the main passivation product in conventional lithium foils. This chemistry agrees with previous results on thin lithium layers prepared by other physical vapor deposition methods such as thermal evaporation [56]. The prolonged storage of PLD-Li prior to analysis likely contributed to the formation of surface oxalates and the transformation of the inner Li<sub>2</sub>O layer, typically found in fresh evaporated lithium foils, into hydroxides, alkoxides or oxalates. Despite this, the presence of this ultrathin passivation layer may provide improved electrochemical stability by minimizing the formation of highly resistive interfacial layers.

# 3.5. Electrochemical performance of PLD Li-on-Cu anodes

With the aim of better understanding the properties of the solid electrolyte - anode interface and to investigate the lithium's electrodeposition/dissolution kinetics, symmetric Li-on-Cu|SE|Li-on-Cu cells were assembled, characterized by means of EIS and subjected to galvanostatic cycling Fig. 4A reports the EIS spectra, normalized by the surface area, recorded at room temperature for symmetric cells assembled with Li-on-Cu layer fabricated by PLD, both with and without the LLZO protective layer. The EIS curves exhibit similar overall trends for both the non-protected and LLZO-protected samples. In the highfrequency region, a semicircle is observed, indicative of charge transfer and bulk resistance contributions, starting from 3 MHz. Then, decreasing the frequency of the impedance contribution arises from either interfacial phenomena or subtle variations in electronic and ionic conduction pathways. Finally, at lower frequencies, the impedance spectrum transitions into a diffusive regime, with the onset of this region occurring at approximately 5 kHz down to 1 Hz. According to this, Fig. 4A also reports the relative fitting with the proposed equivalent circuit composed of a resistor related to bulk contribution, two RC representing respectively grain boundary (gb) and interfacial contribution (int) and a Warburg (W) element.

One of the key challenges in analyzing the impedance response of sulfide-based solid electrolytes lies in distinguishing the bulk resistance ( $R_{bulk}$ ) from the grain boundary resistance ( $R_{gb}$ ), as these two components often exhibit overlapping contributions. The degree of overlap is influenced by various factors, including the specific synthesis method used for the electrolyte, the electrode preparation process, and the testing parameters. However, despite this complexity, the total resistance (defined as the sum of  $R_{bulk}$ ,  $R_{gb}$ , and interfacial resistance  $R_{int}$ ) can still be extracted and compared between the two samples. For the

PLD Li on Cu sample, the total resistance is found to be approximately 70  $\Omega \cdot \text{cm}^2$ , which is significantly reduced to 52  $\Omega \cdot \text{cm}^2$  in the LLZOprotected configuration. This 26 % decrease in total resistance is indicative of improved charge transfer kinetics and reduced interfacial impedance when the LLZO protection layer is present. These observations are confirmed in Table S2, reporting the relative contribution resistance components (R<sub>bulk</sub>, R<sub>gb</sub> and R<sub>int</sub>) according to the fitting with the proposed equivalent circuit. While the R<sub>bulk + gb</sub> associated with PLD\_Li\_on\_Cu\_LLZO is slightly higher than the non-protected sample, the R<sub>int</sub> is sensibly lower. There are several factors contributing to this improvement. First, as confirmed by SEM analysis, the increased surface roughness of the LLZO-protected Li-on-Cu layer promotes superior physical contact and adhesion between the electrode and the solid electrolyte, thereby facilitating more efficient lithium-ion transport across the interface. This reduction in interfacial resistance ( $R_{int}$ ) is a key factor contributing to the overall lower impedance observed for the LLZO-protected sample, highlighting the beneficial role of the protective layer in optimizing electrochemical performance. In addition to that, it must be taken into account that LPSC is very reactive against LiM and it easily decomposes in byproducts such as Li<sub>2</sub>S, P<sub>2</sub>S<sub>5</sub> and polysulfides that are highly resistive and the presence of LLZO layer between LiM helps to reduce LPSC side reactions [37]. Similarly, LLZO may also reduce the amount of resistive Li surface passivation species upon storage. The Distribution of Relaxation Time (DRT) technique was employed to further analyze the EIS spectra of symmetric Li cells, as shown in Fig. 4B. Prior to DRT analysis, the quality and validity of the EIS data were confirmed using the linear Kramers-Kronig (lin\_KK) test, ensuring the absence of experimental artifacts and validating the impedance measurements (Supplementary Material Fig. S4). The DRT analysis (extrapolated in 1st derivative) of PLD\_Li\_on\_Cu reveals 5 distinct peaks, labelled respectively as P1, P2, P3, P4 and P5, each corresponding to different electrochemical processes within the system. P<sub>1</sub> appears at approximately 10<sup>-6</sup> s and is attributed grain boundary response of LPSC sulfide-based solid electrolyte. Peaks  $P_2$  ( $\approx 10^{-3}$  s),  $P_3$  ( $\approx 10^{-2}$  s) and  $P_4$  $(\approx 10^{-1} \text{ s})$  are associated to the resistive-capacitive (RC) charge-transfer processes occurring within the cell at the electrode/electrolyte interface [42,57,58]. Finally, P<sub>5</sub> can be associated with lithium-ion diffusion mechanisms, reflecting transport constraints at the electrode electrolyte interface. Interestingly, the DRT spectrum of the LLZO-protected sample presents some differences. P2, P3 and P4 show increased intensity, suggesting enhanced charge-transfer processes likely due to modifications in the electrode electrolyte interface introduced by the LLZO protective layer. Despite that, P5, linked to ionic diffusion, is significantly attenuated in the LLZO-coated sample, although it remains detectable when data are extracted from the 2<sup>nd</sup> derivative (see Supplementary Fig. S5). This diminished P5 intensity could be attributed to the fact that even if

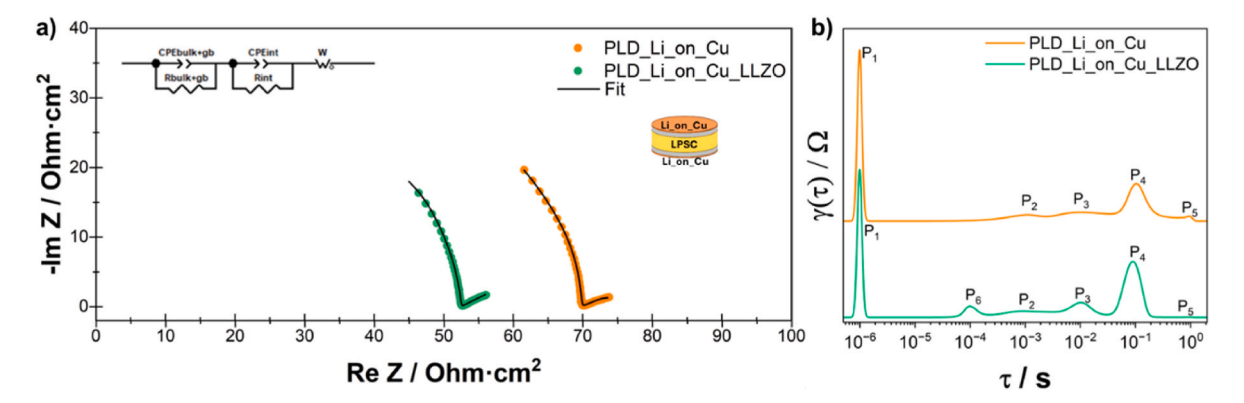


Fig. 4. A): EIS curves of PLD\_Li\_on\_Cu (orange squared) and PLD\_Li\_on\_Cu\_LLZO (green dotted) in symmetric cell configuration. The figure also reports the fitting (solid black line) related to the equivalent circuit proposed together with a scheme of the testing cell configuration. B) DRT of EIS spectra of PLD\_Li\_on\_Cu (solid orange line) and PLD\_Li\_on\_Cu\_LLZO (solid green line) resolved on 1st derivative. (For interpretation of the references to colour in this figure legend, the reader is referred to the Web version of this article.)

LLZO has lower ionic conductivity with respect to the sulfide SE, which can slightly hinder the lithium-ion diffusion the new interfaces are much more stable than the pure SE|LiM. The most significant new feature is the appearance of a new peak,  $P_6$ , at approximately  $10^{-4}$  s. The assignation of this peak is not straightforward, in fact, it could be attributed to interfacial irreversible reactions leading to the formation of SEI [58], but can be also ascribed to grain boundary diffusion in LLZO [59] or to the diffusion in not pure-cubic LLZO phase [60], resulting in an overlapping of different processes. The fact that after assembly this peak is visible only in the PLD\_Li\_on\_Cu\_LLZO, makes it reasonable to attribute it to LLZO, but then, during cycling (see Fig. 5E), it appears also in the non-coated sample with a different evolution over time, confirming the fact that SEI formation and growth also plays a role. However, these findings suggest that while the LLZO layer enhances charge-transfer properties (with more stable interfaces with respect to the non-coated lithium), it may also introduce a new interfacial reaction pathway that may influence the lithium-ion mobility. Fig. 5A-B shows the ST-PT profiles of symmetric cells assembled respectively with PLD Li on Cu and PLD\_Li\_on\_Cu\_LLZO electrodes. Cells were cycled at a current density of 0.1 mA·cm<sup>-2</sup> with a capacity of 0.2 mAh·cm<sup>-2</sup> (2 h per each semi-cycle). The selection of the applied current density was done

according to the CCD tests to be able to cycle the cells in safe conditions for the material (see Fig. S6). The ST-PT profile of the non-protected Li-on-Cu is presented in Fig. 5A, where there is an initial overpotential of around 8 mV. While the stripping and plating profiles remain steady over the first few cycles, the overpotential gradually increases up to 15 mV, accompanied by progressively irregular and noisy steps in the lithium deposition/dissolution process. These effects are probably related to the progressive formation of soft lithium dendrites on both electrode surface [61], leading to the premature short-circuiting of the cell after 100 h of cycling. In fact, one of the degradation mechanisms in LPSC-based SE involves the formation of insulating phases at the SE LiM interface. Sulfides electrolytes, including LPSC, are thermodynamically unstable in contact with LiM, which can lead to the formation of SEI rich in Li<sub>3</sub>P, Li<sub>2</sub>S, and LiCl [62]. These species are more resistive than the bare argyrodite sulfide electrolyte and can accelerate the failure mechanism of the cell by increasing interfacial resistance and promoting uncontrolled dendritic lithium growth. On the other hand, the ST-PT profile of the LLZO-coated PLD Li on Cu electrode reveals a slightly lower initial overpotential and a significantly more stable voltage profile. The overpotential remains nearly constat for the first 60-70 h of cycling before gradually increasing. However, unlike the non-protected

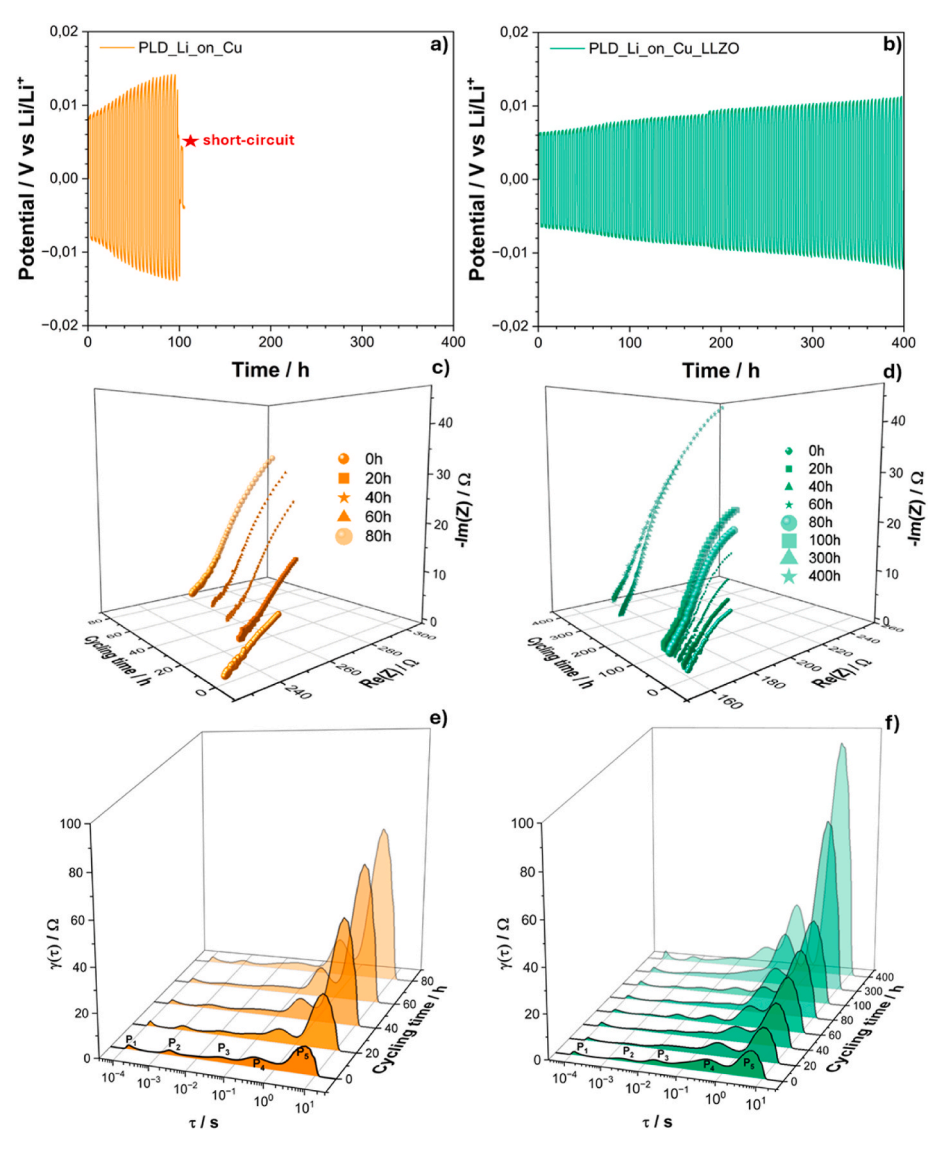


Fig. 5. Electrochemical performance of PLD\_Li\_on\_Cu and PLD\_Li\_on\_Cu\_LLZO. A) ST-PT profile of PLD\_Li\_on\_Cu; B) ST-PT profile of PLD\_Li\_on\_Cu\_LLZO; C) EIS of PLD\_Li\_on\_Cu during ST-PT: D) EIS of PLD\_Li\_on\_Cu\_LLZO during cycling; E) DRT of EIS spectra of PLD\_Li\_on\_Cu during cycling; F) DRT of EIS spectra of PLD\_Li\_on\_Cu\_LLZO during cycling.

electrode, the ST-PT steps remain highly stable up to 400 h. According to these results, it is evident the beneficial role of the LLZO-protective layer deposited. In fact, the symmetric cell with PLD\_Li\_on\_Cu\_LLZO can successfully cycle for more than 400 h before short circuiting with a lower overpotential and with a much more stable profile over time. The improved cycling performance of the LLZO-coated electrode could be attributed to two mains reasons. First, the higher hardness of the LLZO layer of protected electrodes could improve the stacking between LPSC and the negative electrode, reducing the interfacial resistance, as confirmed by EIS. Secondly, as mentioned before, the presence of LLZO as interlayer between LPSC and LiM, could mitigate the degradation kinetics of sulfide electrolyte. This suppression of interfacial degradation contributes to improved stripping-plating performance over time. Fig. 5C-D provide further insights into the evolution of interfacial resistance over cycling time through EIS measurements. In both configurations, an increasing cell resistance is observed during cycling, likely due to the electrode and interface degradation. However, a direct comparison of the first 80 h of cycling reveals that the LLZO-protected PLD Li on Cu electrode consistently exhibits a lower total resistance ( $\approx$ 35 % less) compared to its non-protected counterpart. In addition to that, during this same period the relative increase of the total resistance of the PLD Li on Cu LLZO is much lower ( $\approx$ 3-4 %) with respect to PLD\_Li\_on\_Cu (≈20 %). These findings support the role of LLZO as protective layer by reducing interfacial degradation and preserving effective contact with the LPSC solid electrolyte. Additionally, the low-frequency semicircle in the Nyquist plot, which corresponds to diffusion-related phenomena, becomes more pronounced over time, indicating an increasing contribution from mass transport limitations as the cell ages. To gain further insights into charge transport and interfacial phenomena, the corresponding DRT analyses are presented in Fig. 5E-F. The DRT analysis allows for the deconvolution of different electrochemical processes occurring in the cell, providing a more detailed understanding of the resistance evolution. Consistent with the EIS results, the peaks corresponding to diffusion-related processes, which appear in the  $10^0$ – $10^1$  s region (P<sub>4</sub> and P<sub>5</sub>), display an increasing intensity over time, indicative of higher mass transport limitations. Similarly, peaks associated with charge-transfer and interfacial phenomena, within the  $10^{-3}$ – $10^{-1}$  s range (P<sub>2</sub> and P<sub>3</sub>), also exhibit a steady increase in intensity over time. Finally, P1, related to SEI formation and growing over time, is more pronounced in the non-protected PLD Li on Cu electrode, further confirming the accelerated interfacial degradation in this configuration. Conversely, the LLZO-coated electrode displays a more gradual increase in resistance, consistent with its enhanced stability as observed in both the ST-PT profiles and EIS spectra (Fig. 5C-D). Overall, the electrochemical characterization presented in Fig. 5 underscores the advantages of LLZO as a protective interlayer for Li\_on\_Cu electrodes. The presence of LLZO not only reduces initial interfacial resistance, but also significantly improves the long-term cycling stability of symmetric cells by mitigating interfacial

degradation and suppressing lithium dendrite formation. The effectiveness of the LLZO layer is further demonstrated by additional stability tests that were carried out in symmetric cells without applying any current over more than 90 days. Fig. S7 in the supplementary material shows how both the bare and LLZO-coated PLD anodes are quite stable with time but the total resistance and the relative increase over time of the PLD Li on Cu LLZO is lower with respect to PLD Li on Cu.

To evaluate the effectiveness of LiMA with a LLZO protective layer, CR2032 coin cells were assembled incorporating an LPSC solid electrolyte and a composite NMC90505-based cathode. For comparative analysis, commercial LiM foil and PLD-prepared Li-on-Cu anodes were employed. Fig. 6A illustrates the evolution of the first charge/discharge voltage curve for the full cells assembled with different PLD LiMA. Under a constant current of 0.05C, the cell with the thin PLD Li on -Cu LLZO delivered a specific capacity of 187 mAh·g<sup>-1</sup>, with a Coulombic efficiency (CE) of 71 %, that is comparable to select reports in the literature on ASSBs incorporating thin LiMA, sulfide-based SE, and layered oxide NMC cathodes [8]. In contrast, the full cell assembled with PLD Li on Cu exhibited voltage instability above 4.1 V (vs Li/Li<sup>+</sup>) during the charging process and failed to reach the upper cut-off voltage of 4.3 V (vs Li/Li<sup>+</sup>). Such behavior has been already reported as dendrite formation during the Li plating step [15,36,63]. The improvement observed for the LLZO-protected anode is likely due to the formation of a more stable and less resistive SEI, primarily composed of inorganic species derived from LLZO [36]. This SEI mitigates the formation of soft Li dendrites during charging in full cell configuration and in agreement with the results from symmetric cells, thereby improving cycling stability. Projected energy density calculations presented in this work indicate that reducing the LiMA thickness from 100 µm to 10 µm yields a modest yet measurable improvement in both gravimetric and volumetric energy densities. Specifically, the gravimetric energy density (Eg) increases from 44.5 Wh·kg<sup>-1</sup> to 45.8 Wh·kg<sup>-1</sup>, while the volumetric energy density ( $E_v$ ) improves from 80.4 Wh·l<sup>-1</sup> to 88.4 Wh·l<sup>-1</sup>. These estimations are based on a fixed cathode composition of 57:40:3 wt% NMC90505:LPSCl:C65 and an 800 µm-thick sulfide-based solid electrolyte separator, selected for internal comparison reasons. Notably, further improvements in energy densities could be achieved by increasing the cathode areal capacity from 2 mAh·cm<sup>-2</sup> to 4 mAh·cm<sup>-</sup> raising E<sub>g</sub> and E<sub>v</sub> to projected values of 81.7 Wh·kg<sup>-1</sup> and 164.1 Wh·l<sup>-1</sup> respectively. More substantial gains are attainable when adopting parameters aligned with industrially relevant configurations, as shown in Fig. 6B. For example, employing a cathode composed of 80:15:3:2 wt% NMC90505:LPSCl:C65:Binder with a practical loading of 4 mAh·cm<sup>-2</sup>, combined with a 40 µm-thick LPSC separator and a 10 µm-thick LiM, results in projected energy densities of 274 Wh·kg<sup>-1</sup> and 959 Wh·l<sup>-1</sup> These assumptions underscore the strong potential of PLD-fabricated LiMA architectures for enabling high-performance ASSBs capable of meeting industrial demands.

With the aim of evaluating the scalability of PLD LiMA for larger

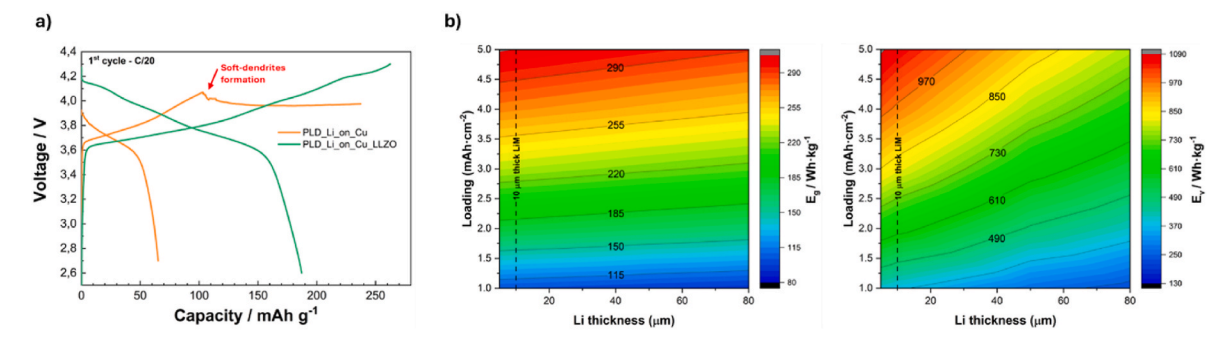


Fig. 6. A) Constant current charge/discharge profile at C-rate of C/20 of full cells assembled against PLD\_Li\_on\_Cu\_LLZO and a commercial Li foil as comparison; B) Gravimetric ( $E_y$ ) and Volumetric ( $E_y$ ), energy densities evolution versus Li thickness and cathode loading (projected energy density estimations assume 80:15:3:2 wt% NMC90505:LPSCl:C65:Binder cathode composition and an 40  $\mu$ m-thick sulfide-based SE).

scale applications with respect to lab-scale, full cells were also assembled coupling the anodes with different types of wet processed NMC-based cathodes. Galvanostatic cycling, cyclic voltammetry and electrochemical impedance spectroscopy were performed, and preliminary results are presented in the supplementary material (Figs. S8 and S9).

#### 4. Conclusions

This study demonstrates that PLD is a powerful and versatile technique for the fabrication of LiMA in ASSBs. The precision of PLD enables the deposition of uniform, high-purity LiM layers directly onto Cu substrates, while also allowing for the sequential deposition of functional protective layers within a single process. Comprehensive structural, microstructural and compositional analysis confirms the effectiveness of PLD deposition technique, revealing the formation of a thin passivation layer with distinct characteristics compared to conventional LiM obtained via mechanical processing. Additionally, the successful deposition of a thin, partially cubic LLZO coating layer via PLD highlights the potential of the manufacturing method for ad-hoc interfacial engineering. Both the non-protected and LLZO-protected anodes were subsequently evaluated in symmetric cell configuration, demonstrating the significant advantages conferred by the LLZO coating. Electrochemical testing revealed the role of the LLZO interlayer in enhancing both interface stability over long times and cycling stability, characterized by lower overpotential and extended cycling life compared to bare lithium anodes. EIS and DRT analysis further validated the enhanced interfacial kinetics provided by the LLZO layer, underscoring its role in improving lithium-ion transport and mitigating interfacial degradation. To assess practical applicability, the LLZO-coated LiMA was integrated into full cells with an NMC955-based cathode. The results affirm the potential of PLD as a scalable and effective fabrication technique for LiMA, offering promising electrochemical performance and improved stability. In particular, the technique supports lean-lithium designs by enabling the deposition of lithium with minimal excess,an essential requirement for achieving high gravimetric and volumetric energy densities. Moreover, the flexibility of PLD in shaping lithium layers into a variety of geometries and configurations allows for the development of customized cell architectures beyond the constraints of conventional processing methods. Future research should focus on optimizing deposition parameters to improve film uniformity, interfacial adhesion, and long-term stability. Additionally, further investigations into the integration of PLDfabricated anodes in full cell architectures will be essential for advancing their commercial viability and pave the way for the development of high-performance ASSBs, advancing the commercialization of nextgeneration energy storage technologies.

# CRediT authorship contribution statement

Nico Zamperlin: Writing – review & editing, Writing – original draft, Visualization, Validation, Methodology, Formal analysis, Data curation. Rosalía Cid: Writing – review & editing, Investigation, Formal analysis, Data curation. Ville Kekkonen: Writing – review & editing, Validation, Resources, Investigation, Funding acquisition. Arianna Pesce: Writing – review & editing, Investigation. Manar Cheddadi: Investigation. Beatriz M. Gomes: Writing – review & editing, Validation, Investigation. Manuela C. Baptista: Writing – review & editing, Validation, Investigation. M. Helena Braga: Writing – review & editing, Investigation, Funding acquisition. Ander Orue: Writing – review & editing, Writing – original draft, Visualization, Validation, Supervision, Project administration, Methodology, Investigation, Conceptualization. Pedro López-Aranguren: Writing – review & editing, Visualization, Supervision, Resources, Funding acquisition, Conceptualization.

# Declaration of competing interest

The authors declare the following financial interests/personal

relationships which may be considered as potential competing interests: Ander Orue reports financial support was provided by European Union. If there are other authors, they declare that they have no known competing financial interests or personal relationships that could have appeared to influence the work reported in this paper.

### Acknowledgments

This project has received funding from the European Union's Horizon Europe research and innovation programme under grant agreement No. 101069686 (PULSELION). Views and opinions expressed are those of the author(s) only and do not necessarily reflect those of the European Union or CINEA. Neither the European Union nor the granting authority can be held responsible for them. The authors would like to thank Dr. Yan Zhang for her contribution in performing Raman analysis. The authors also acknowledge the collaboration between Pulsedeon Oy and Tampere University within the framework of the national Business Finland project called NextGenBat.

# Appendix A. Supplementary data

Supplementary data to this article can be found online at https://doi.org/10.1016/j.jpowsour.2025.237986.

# Data availability

Data will be made available on request.

#### References

- F. Zheng, M. Kotobuki, S. Song, M.O. Lai, L. Lu, Review on solid electrolytes for allsolid-state lithium-ion batteries, J. Power Sources 389 (2018) 198–213, https:// doi.org/10.1016/j.jpowsour.2018.04.022.
- [2] R. Murugan, W. Weppner (Eds.), Solid Electrolytes for Advanced Applications: Garnets and Competitors, Springer International Publishing, Cham, 2019, https://doi.org/10.1007/978-3-030-31581-8
- [3] B. Tao, D. Zhong, H. Li, G. Wang, H. Chang, Halide solid-state electrolytes for all-solid-state batteries: structural design, synthesis, environmental stability, interface optimization and challenges, Chem. Sci. 14 (2023) 8693–8722, https://doi.org/10.1030/D3SC/020938
- [4] P. López-Aranguren, P. Lannelongue, J. Carrasco, A. Golov, A. Robles-Fernandez, E. Gonzalo, A. Tron, T. Marchandier, A.-K. Hatz, R. Fathi, Q. Xu, D. Chaykina, C. A. Varkey, C. Gavagnin, M. Kaminski, A. Almousli, G.G. Eshetu, N. Hamzelui, F. Diaz, E. Drude, S. Abada, N. Guy, A. Sudharshan, M. Brunetti, S. Beschnitt, HELENA project: driving innovation in high energy density Li-metal halide solid-state batteries for electric vehicles and aircrafts, Comput. Struct. Biotechnol. J. 29 (2025) 72–84, https://doi.org/10.1016/j.csbj.2025.03.013.
- [5] D. Ren, L. Lu, R. Hua, G. Zhu, X. Liu, Y. Mao, X. Rui, S. Wang, B. Zhao, H. Cui, M. Yang, H. Shen, C.-Z. Zhao, L. Wang, X. He, S. Liu, Y. Hou, T. Tan, P. Wang, Y. Nitta, M. Ouyang, Challenges and opportunities of practical sulfide-based all-solid-state batteries, eTransportation 18 (2023) 100272, https://doi.org/10.1016/j.etran.2023.100272.
- [6] C. Xu, L. Chen, F. Wu, Unveiling the power of sulfide solid electrolytes for next-generation all-solid-state lithium batteries, Next Mater. 6 (2025) 100428, https://doi.org/10.1016/j.nxmate.2024.100428.
- [7] Y.-G. Lee, S. Fujiki, C. Jung, N. Suzuki, N. Yashiro, R. Omoda, D.-S. Ko, T. Shiratsuchi, T. Sugimoto, S. Ryu, J.H. Ku, T. Watanabe, Y. Park, Y. Aihara, D. Im, I.T. Han, High-energy long-cycling all-solid-state lithium metal batteries enabled by silver-carbon composite anodes, Nat. Energy 5 (2020) 299–308, https://doi. org/10.1038/s41560-020-0575-z.
- [8] K. Schönherr, B. Schumm, F. Hippauf, R. Lissy, H. Althues, C. Leyens, S. Kaskel, Liquid lithium metal processing into ultrathin metal anodes for solid state batteries, Chem. Eng. J. Adv. 9 (2022) 100218, https://doi.org/10.1016/j. ceia.2021.100218.
- [9] Y. Zhang, T.-T. Zuo, J. Popovic, K. Lim, Y.-X. Yin, J. Maier, Y.-G. Guo, Towards better li metal anodes: challenges and strategies, Mater. Today 33 (2020) 56–74, https://doi.org/10.1016/j.mattod.2019.09.018.
- [10] N. Liu, W. Li, M. Pasta, Y. Cui, Nanomaterials for electrochemical energy storage, Front. Physiol. 9 (2014) 323–350, https://doi.org/10.1007/s11467-013-0408-7.
- [11] M. Burton, S. Narayanan, B. Jagger, L.F. Olbrich, S. Dhir, M. Shibata, M.J. Lain, R. Astbury, N. Butcher, M. Copley, T. Kotaka, Y. Aihara, M. Pasta, Technoeconomic assessment of thin lithium metal anodes for solid-state batteries, Nat. Energy 10 (2024) 135–147, https://doi.org/10.1038/s41560-024-01676-7.
- [12] D. Karabelli, K.P. Birke, Feasible energy density pushes of Li-Metal vs. Li-Ion cells, Appl. Sci. 11 (2021) 7592, https://doi.org/10.3390/appl.1167592.
- [13] D.K. Singh, A. Henss, B. Mogwitz, A. Gautam, J. Horn, T. Krauskopf, S. Burkhardt, J. Sann, F.H. Richter, J. Janek, Li<sub>6</sub>PS<sub>5</sub>Cl microstructure and influence on dendrite

- growth in solid-state batteries with lithium metal anode, Cell Rep. Phys. Sci. 3 (2022) 101043, https://doi.org/10.1016/j.xcrp.2022.101043.
- [14] H. Liu, W. Jiang, W. Chen, Q. Lin, S. Ren, Y. Su, R. Tong, Y. Zhang, Dendrite growth and inhibition in all-solid-state lithium metal batteries: in Situ optical observation, J. Mater. Chem. A 12 (2024) 3575–3579, https://doi.org/10.1039/D3TA07366A.
- [15] P. López-Aranguren, X. Judez, M. Chakir, M. Armand, L. Buannic, High voltage solid state batteries: targeting high energy density with polymer composite electrolytes, J. Electrochem. Soc. 167 (2020) 020548, https://doi.org/10.1149/ 1945-7111/ab6dd7
- [16] J. Li, J. Luo, X. Li, Y. Fu, J. Zhu, X. Zhuang, Li metal anode interface in sulfide-based all-solid-state L i batteries, EcoMat 5 (2023) e12383, https://doi.org/ 10.1002/eom2.12383
- [17] J.-C. Wang, L.-L. Zhao, N. Zhang, P.-F. Wang, T.-F. Yi, Interfacial stability between sulfide solid electrolytes and lithium anodes: challenges, strategies and perspectives, Nano Energy 123 (2024) 109361, https://doi.org/10.1016/j. nanoen.2024.109361.
- [18] R. Rajagopal, Y. Subramanian, S. Kang, J. Park, K.-S. Ryu, Improved interfacial stability of all-solid-state batteries using cation-anion co-doped glass electrolytes, Commun Mater 5 (2024) 78, https://doi.org/10.1038/s43246-024-00514-3.
- [19] G. Yoon, S. Kim, J. Kim, Design strategies for anodes and interfaces toward practical solid-state li-metal batteries, Adv. Sci. 10 (2023) 2302263, https://doi. org/10.1002/advs.202302263.
- [20] J. Li, Y. Li, J. Cheng, Q. Sun, L. Dai, N. Ci, D. Li, L. Ci, In situ modified sulfide solid electrolyte enabling stable lithium metal batteries, J. Power Sources 518 (2022) 230739, https://doi.org/10.1016/j.jpowsour.2021.230739.
- [21] L. Fallarino, U.N. Chishti, A. Pesce, G. Accardo, A. Rafique, M. Casas-Cabanas, P. López-Aranguren, Towards lithium-free solid-state batteries with nanoscale Ag/ Cu sputtered bilayer electrodes, Chem. Commun. 59 (2023) 12346–12349, https://doi.org/10.1039/D3CC02942E.
- [22] P. Bouchard, P.E. Guerin, G. St-Amant, G. Laroche, Thin film lithium rolling method with controlled separation, CA Patent CA2099524C (1999).
- [23] Y. Masayoshi, K. Takeshi, S. Kentaro, N. Taichi, K. Takeyuki, Rolling method of lithium foil, JP Patent, JP2018130759A (2018).
- [24] D. Vanleeuw, D. Sapundjiev, G. Sibbens, S. Oberstedt, P. Salvador Castiñeira, Physical vapour deposition of metallic lithium, J. Radioanal. Nucl. Chem. 299 (2014) 1113–1120, https://doi.org/10.1007/s10967-013-2669-6.
- [25] A. Rafique, L. Fallarino, G. Accardo, A. Pesce, F. Bonilla, Y. Zhang, S. Lanceros-Mendez, M. Casas-Cabanas, P. López-Aranguren, Interfacial analysis of in-situ anode formation in solid-state batteries with nanometric current collector, Chem. Eng. J. 509 (2025) 160956, https://doi.org/10.1016/j.cej.2025.160956.
- [26] H.-U. Krebs, M. Weisheit, J. Faupel, E. Süske, T. Scharf, C. Fuhse, M. Störmer, K. Sturm, M. Seibt, H. Kijewski, D. Nelke, E. Panchenko, M. Buback, Pulsed laser deposition (PLD) – A versatile thin film technique, in: B. Kramer (Ed.), Advances in Solid State Physics, Springer Berlin Heidelberg, Berlin, Heidelberg, 2003, pp. 505–518, https://doi.org/10.1007/978-3-540-44838-9 36.
- [27] M.J. Aziz, Film growth mechanisms in pulsed laser deposition, Appl. Phys. A 93 (2008) 579–587, https://doi.org/10.1007/s00339-008-4696-7.
- [28] M. Saccoccio, J. Yu, Z. Lu, S.C.T. Kwok, J. Wang, K.K. Yeung, M.M.F. Yuen, F. Ciucci, Low temperature pulsed laser deposition of garnet Li<sub>6.4</sub>La<sub>3</sub>Zr<sub>1.4</sub>Ta<sub>0.6</sub>O<sub>12</sub> films as all solid-state lithium battery electrolytes, J. Power Sources 365 (2017) 43–52, https://doi.org/10.1016/j.jpowsour.2017.08.020.
- [29] J. Kriegler, E. Jaimez-Farnham, L. Hille, E. Dashjav, M.F. Zaeh, Pulsed laser ablation of a ceramic electrolyte for all-solid-state batteries, Proced. CIRP 111 (2022) 800–805, https://doi.org/10.1016/j.procir.2022.08.132.
- [30] J. Kriegler, T.M. Duy Nguyen, L. Tomcic, L. Hille, S. Grabmann, E.I. Jaimez-Farnham, M.F. Zaeh, Processing of lithium metal for the production of post-lithium-ion batteries using a pulsed nanosecond fiber laser, Results Mater. 15 (2022) 100305, https://doi.org/10.1016/j.rinma.2022.100305.
- [31] M. Fenech, N. Sharma, Pulsed laser deposition-based thin film microbatteries, Chem. Asian J. 15 (2020) 1829–1847, https://doi.org/10.1002/asia.202000384.
- [32] L. Indrizzi, N. Ohannessian, D. Pergolesi, T. Lippert, E. Gilardi, Pulsed laser deposition as a tool for the development of all solid-state microbatteries, Helv. Chim. Acta 104 (2021) e2000203, https://doi.org/10.1002/hlca.202000203.
- [33] W. Wang, Y. Li, L. Li, L. Wang, K. Wang, SnO<sub>2</sub>/TiO<sub>2</sub> nanocomposite prepared by pulsed laser deposition as anode material for flexible quasi-solid-state lithium-ion batteries, Int. J. Electrochem. Sci. 15 (2020) 11709–11722, https://doi.org/ 10.20964/2020.12.49.
- [34] L. Cao, D. Wang, R. Wang, NiO thin films grown directly on Cu foils by pulsed laser deposition as anode materials for lithium ion batteries, Mater. Lett. 132 (2014) 357–360, https://doi.org/10.1016/j.matlet.2014.06.114.
- [35] L. Gireaud, S. Grugeon, S. Laruelle, B. Yrieix, J.-M. Tarascon, Lithium metal stripping/plating mechanisms studies: a metallurgical approach, Electrochem. Commun. 8 (2006) 1639–1649, https://doi.org/10.1016/j.elecom.2006.07.037.
- [36] A. Orue, M. Arrese-Igor, R. Cid, X. Júdez, N. Gómez, J.M. López Del Amo, W. Manalastas, M. Srinivasan, C. Rojviriya, M. Armand, F. Aguesse, P. López-Aranguren, Enhancing the polymer electrolyte–Li metal interface on high-voltage solid-state batteries with Li-based additives inspired by the surface chemistry of Li<sub>7</sub> La<sub>3</sub> Zr<sub>2</sub> O<sub>12</sub>, J. Mater. Chem. A 10 (2022) 2352–2361, https://doi.org/10.1039/ D1TAGS2626
- [37] L. Merola, V.K. Singh, M. Palmer, J.K. Eckhardt, S.L. Benz, T. Fuchs, L.F. Nazar, J. Sakamoto, F.H. Richter, J. Janek, Evaluation of oxide|sulfide heteroionic interface stability for developing solid-state batteries with a lithium-metal electrode: the case of LLZO|Li<sub>0</sub>PS<sub>5</sub>Cl and LLZO|Li<sub>7</sub>P<sub>3</sub>S<sub>11</sub>, ACS Appl. Mater. Interfaces 16 (2024) 54847–54863, https://doi.org/10.1021/acsami.4c11597.

- [38] J. Gerstenberg, D. Steckermeier, A. Kwade, P. Michalowski, Effect of mixing intensity on electrochemical performance of oxide/sulfide composite electrolytes, Batteries 10 (2024) 95, https://doi.org/10.3390/batteries10030095.
- [39] J.H. Scofield, Theoretical photoionization cross sections from 1 to 1500 keV, Lawrence Livermore Laboratory Reports UCRL - 51326, Livermore, Ca (1973).
- [40] M.P. Seah, Simple universal curve for the energy-dependent electron attenuation length for all materials, Surf. Interface Anal. 44 (2012) 1353–1359, https://doi. org/10.1002/cia.5033
- [41] A. Beutl, A. Orue, P. López-Aranguren, A. Itziar Pitillas Martinez, M.H. Braga, V. Kekkonen, A. Tron, Round-robin test of all-solid-state battery with sulfide electrolyte assembly in coin-type cell configuration, Electrochem. Sci. Adv. (2024) e2400004, https://doi.org/10.1002/elsa.202400004.
- [42] A. Orue Mendizabal, M. Cheddadi, A. Tron, A. Beutl, P. López-Aranguren, Understanding interfaces at the positive and negative electrodes on sulfide-based solid-state batteries, ACS Appl. Energy Mater. 6 (2023) 11030–11042, https://doi. org/10.1021/acsaem.3c01894.
- [43] A. Anderson, F. Lüty, Raman scattering, defect luminescence, and phonon spectra of <sup>7</sup>LiH, <sup>6</sup>LiH, and <sup>7</sup>LiD crystaLs, Phys. Rev. B 28 (1983) 3415–3421, https://doi. org/10.1103/PhysRevB.28.3415.
- [44] Y. Hase, I.V. Pagotto Yoshida, The raman active vibrational modes and isotopic effects of four isotopically substituted lithium hydroxides, Chem. Phys. Lett. 65 (1979) 46–49, https://doi.org/10.1016/0009-2614(79)80122-0.
- [45] Y. Lshii, T. Nagasaki, N. Igawa, H. Watanabe, H. Ohno, Temperature dependence of the raman spectrum in lithium oxide single crystal, J. Am. Ceram. Soc. 74 (1991) 2324–2326, https://doi.org/10.1111/j.1151-2916.1991.tb08308.x.
- [46] C. Naudin, J.L. Bruneel, M. Chami, B. Desbat, J. Grondin, J.C. Lassègues, L. Servant, Characterization of the lithium surface by infrared and raman spectroscopies, J. Power Sources 124 (2003) 518–525, https://doi.org/10.1016/ S0338-7753(03)00798-5
- [47] J.H. Yates, R.M. Pitzer, A b i n i t i o geometry and vibrational frequencies for lithium peroxide, J. Chem. Phys. 66 (1977) 3592–3597, https://doi.org/10.1063/ 1.434393.
- [48] G. Perna, Vibrational characterization of synthetic eumelanin by means of raman and surface enhanced raman scattering, TOSURSJ 5 (2013) 1–8, https://doi.org/ 10.2174/1876531901305010001.
- [49] Y. Hase, I.V.P. Yoshida, Raman and infrared spectra of 6Li<sub>2</sub>C<sub>2</sub>O<sub>4</sub> and 7Li<sub>2</sub>C<sub>2</sub>O<sub>4</sub>, Monatsh. Chem. 111 (1980) 1265–1272, https://doi.org/10.1007/BF00903653.
- [50] F. Tietz, T. Wegener, M.T. Gerhards, M. Giarola, G. Mariotto, Synthesis and raman micro-spectroscopy investigation of Li<sub>2</sub>La<sub>3</sub>Zr<sub>2</sub>O<sub>12</sub>, Solid State Ionics 230 (2013) 77–82, https://doi.org/10.1016/j.ssi.2012.10.021.
- [51] J.S. Park, L. Cheng, V. Zorba, A. Mehta, J. Cabana, G. Chen, M.M. Doeff, T. J. Richardson, J.H. Park, J.-W. Son, W.-S. Hong, Effects of crystallinity and impurities on the electrical conductivity of li–la–zr–o thin films, Thin Solid Films 576 (2015) 55–60, https://doi.org/10.1016/j.tsf.2014.11.019.
- [52] T. Thompson, J. Wolfenstine, J.L. Allen, M. Johannes, A. Huq, I.N. David, J. Sakamoto, Tetragonal vs. cubic phase stability in Al – free Ta doped Li<sub>2</sub>La<sub>3</sub>Zr<sub>2</sub>O<sub>12</sub> (LLZO), J. Mater. Chem. A 2 (2014) 13431–13436, https://doi.org/10.1039/ C4TA02099F.
- [53] M. Rawlence, I. Garbayo, S. Buecheler, J.L.M. Rupp, On the chemical stability of post-lithiated garnet Al-stabilized Li<sub>7</sub>La<sub>3</sub>Zr<sub>2</sub>O<sub>12</sub> solid state electrolyte thin films, Nanoscale 8 (2016) 14746–14753, https://doi.org/10.1039/C6NR04162K.
- [54] P. Ghorbanzade, A. Pesce, K. Gómez, G. Accardo, S. Devaraj, P. López-Aranguren, J.M. López Del Amo, Impact of thermal treatment on the Li-ion transport, interfacial properties, and composite preparation of LLZO garnets for solid-state electrolytes, J. Mater. Chem. A 11 (2023) 11675–11683, https://doi.org/10.1039/ D3TA01145C.
- [55] A. Etxebarria, S.L. Koch, O. Bondarchuk, S. Passerini, G. Teobaldi, M.Á. Muñoz-Márquez, Work function evolution in li anode processing, Adv. Energy Mater. 10 (2020) 2000520, https://doi.org/10.1002/aenm.202000520.
- [56] B. Acebedo, R. Cid, M. De Lasen-Tejada, M.C. Morant-Miñana, L. Fallarino, E. Goikolea, J. Rikarte, E. Gonzalo, I. Ruiz De Larramendi, On the role of ultrathin lithium metal anodes produced by thermal evaporation, J. Power Sources 618 (2024) 235218, https://doi.org/10.1016/j.jpowsour.2024.235218.
- [57] C. Plank, T. Rüther, L. Jahn, M. Schamel, J.P. Schmidt, F. Ciucci, M.A. Danzer, A review on the distribution of relaxation times analysis: a powerful tool for process identification of electrochemical systems, J. Power Sources 594 (2024) 233845, https://doi.org/10.1016/j.jpowsour.2023.233845.
- [58] L. Zhang, Y. Dai, C. Li, Y. Dang, R. Zheng, Z. Wang, Y. Wang, Y. Cui, H. Arandiyan, Z. Shao, H. Sun, Q. Zhuang, Y. Liu, Recent advances in electrochemical impedance spectroscopy for solid-state batteries, Energy Storage Mater. 69 (2024) 103378, https://doi.org/10.1016/j.ensm.2024.103378.
- [59] O. Cojocaru-Mirédin, J. Schmieg, M. Müller, A. Weber, E. Ivers-Tiffée, D. Gerthsen, Quantifying lithium enrichment at grain boundaries in Li<sub>7</sub>La<sub>3</sub>Zr<sub>2</sub>O<sub>12</sub> solid electrolyte by correlative microscopy, J. Power Sources 539 (2022) 231417, https://doi.org/10.1016/j.jpowsour.2022.231417.
- [60] Y.-J. Zhou, Y.-Q. Zhou, X.-Y. Li, H. Zhou, X. Huang, B. Tian, Distribution of relaxation times assisted grain and grain boundary structural diagnosis of La<sub>2</sub>Zr<sub>2</sub>O<sub>7</sub>-modified Al-doped Li<sub>7</sub>La<sub>3</sub>Zr<sub>2</sub>O<sub>12</sub> solid electrolyte, Rare Met. 44 (2025) 3037–3050, https://doi.org/10.1007/s12598-024-03068-y.
- [61] S.-Y. Ham, H. Yang, O. Nunez-cuacuas, D.H.S. Tan, Y.-T. Chen, G. Deysher, A. Cronk, P. Ridley, J.-M. Doux, E.A. Wu, J. Jang, Y.S. Meng, Assessing the critical

- current density of all-solid-state li metal symmetric and full cells, Energy Storage
- Mater. 55 (2023) 455–462, https://doi.org/10.1016/j.ensm.2022.12.013.
  [62] S. Wenzel, S.J. Sedlmaier, C. Dietrich, W.G. Zeier, J. Janek, Interfacial reactivity and interphase growth of argyrodite solid electrolytes at lithium metal electrodes, Solid State Ionics 318 (2018) 102–112, https://doi.org/10.1016/j.ssi.2017.07.005.
- [63] G. Homann, L. Stolz, J. Nair, I.C. Laskovic, M. Winter, J. Kasnatscheew, Poly (Ethylene oxide)-based electrolyte for solid-state-lithium-batteries with high voltage positive electrodes: evaluating the role of electrolyte oxidation in rapid cell failure, Sci. Rep. 10 (2020) 4390, https://doi.org/10.1038/s41598-020-61373-9.